IOP Conf. Series: Materials Science and Engineering **1345** (2026) 012004 doi:10.1088/1757-899X/1345/1/012004

Investigating the Microstructure of Cold-Worked and Annealed SRF Niobium Using Shannon Entropy

T Boritz[1,2*], S Balachandran[1,3], S Chetri[1], P J Lee[1], E M Taleff[4] and P Eisenlohr[5]

[1] Applied Superconductivity Center, National High Magnetic Field Laboratory, Florida State University, Tallahassee, FL 32310, USA
[2] Department of Physics, College of Arts and Sciences, Florida State University, Tallahassee, FL 32306, USA
[3] Department of Mechanical Engineering, FAMU-FSU College of Engineering, Florida State University, Tallahassee, FL 32310, USA
[4] Walker Department of Mechanical Engineering, The University of Texas at Austin, Austin, TX 78712, USA
[5] Chemical Engineering and Materials Science, Michigan State University, East Lansing, MI 48824, USA

E-mail: tmb22a@fsu.edu

Abstract. Residual trapped magnetic flux suppresses the quality factor of superconducting radio frequency (SRF) Nb cavities. This makes microstructural features that can trap flux, such as grain boundaries and lattice dislocations, particularly interesting for developing higher cavity performance. The standard technique of electron backscatter diffraction (EBSD) mapping on polished cross sections can quantify these features, but it is expensive and slow, particularly for large scan areas. Backscatter electron (BSE) contrast imaging can be a less expensive and faster alternative, but the large and heterogeneous lattice distortions present in cold-worked Nb challenge standard BSE image analysis techniques. Shannon entropy maps of BSE images are investigated as a potential tool for quantifying Nb microstructures developed during different processing paths. We report on 1) the entropy of BSE images of heat-treated Nb ranging from as-received (cold-worked) to fully recrystallized after annealing at 900 °C for 3 h, 2) methods to find the most effective values for adjustable parameters for entropy calculation, and 3) a comparison of measurements for the recrystallized microstructure fraction derived from EBSD data and BSE entropy maps.

1 Introduction

Among the most significant challenges to improving the performance of superconducting radio frequency (SRF) cavities made of Nb is minimizing defects in the bulk Nb microstructure that lead to trapped magnetic flux, increased overall resistance, and thus suppress the efficiency of the resonator cavity as specified by its quality factor (Q_0). The higher Q_0 the better is the overall cryogenic efficiency, and the lower is the load on the helium cryogenic plant for operating SRF cryomodules with Nb-based cavities at temperatures below 2 K.

Prior investigations have demonstrated that microstructure defects, grain boundaries, and dislocations can trap flux[1]. For example, it was recently observed[2] that grain sizes of 10 µm to 50 µm lead to more flux-trapping than larger grain sizes of 100 µm to 400 µm. Obtaining a complete recrystallization (RX)

by eliminating regions of high dislocation density and promoting consistent grain growth after cavity fabrication and heat treatment in SRF cavities leads to improved flux expulsion [3] and is a high priority.

Measuring grain size and the degree of RX in metals are two of the oldest and most important problems in metallurgical science. Both are fundamentally about distinguishing regions of crystal lattice disorder. Grain size is measured by first distinguishing grain boundaries, which are regions of abrupt lattice reorientation; each grain is nominally a small single crystal with a lattice orientation different from its neighbors. RX is the growth of new grains that have low residual dislocation content into a deformed microstructure with a high dislocation content. RX is typically produced by heavily cold working a metal and then annealing it at a temperature sufficiently high to induce RX instead of just recovery (RV). RV produces a more modest reduction in dislocation density during annealing than does RX [4]. Differentiating RX from RV requires differentiating between very low and only moderate dislocation densities, an often difficult task [5]. Doing this successfully on large spatial scales is especially important because recent results demonstrated that assembling SRF cavities from cold-worked Nb sheets instead of annealed sheets can make it easier to reduce flux-trapping during subsequent heat treatments [3].

Electron backscatter diffraction (EBSD) is generally the most accurate means of both detecting grain boundaries and measuring lattice deformation gradients with sufficient accuracy to distinguish RX from RV, especially when high-angular resolution techniques are applied [6]. However, acquiring EBSD data can be expensive and slow, especially when large scan areas are required. Because backscatter electron (BSE) imaging can produce sufficient channeling and contrast due to misorientations inside grains and orientation changes between grains that enable differentiating between microstructures produced by RX and RV, it can offer a less expensive and faster alternative to EBSD. However, BSE images produced through traditional techniques, which use only a single imaging condition, cannot necessarily be used to identify all grain boundaries or distinguish all regions with retained lattice deformation, *i.e.*, subjected to RV but not RX. Bennett and Taleff [6] addressed this shortcoming by acquiring multiple BSE images from a single field, each with a slightly different tilt relative to the electron beam and detector. Because BSE contrast is very sensitive to imaging conditions, simply varying specimen tilt by 1 to 2° can be sufficient to reveal all individual grains by diffraction contrast, even if similar in orientation. When three different tilts of −1, 0, and 1° are used to produce three images of the same field, these can be conveniently colorized on a red-green-blue (RGB) scale to visualize as a single color image. This technique of using multiple BSE images from a single field is termed combined backscatter electron (CBSE) imaging [6].

The present study builds on this previous work to quantify microstructure—specifically local crystal lattice disorder—using BSE images of large Nb microstructure cross-sections [7]. We develop methods to identify the microstructure of the defect or disorder as a measure of the Shannon information entropy of the BSE signal and evaluate the applicability of this technique to measure the degree of RX of Type 5 (high purity) Nb material [8] typical of that used to produce SRF cavities.

2 Experimental Methods

2.1 Sample Preparation

The Nb samples used in this study are extracted from two Nb sheets provided by ATI, cold-rolled to 40 % and 70 % reduction, with final thicknesses of 7.5 mm and 2.8 mm, respectively. Specimens for microstructural characterization by scanning electron microscopy were cut from the two sheets using wire electron-discharge machining to rectangular coupons. For heat treatment, the coupons were sealed in quartz tubes filled with 400 mTorr Argon gas and heat-treated to 700, 800, and 900 °C for 3 h. The samples are then embedded in conductive metallographic mounts. The cross-sectional plane normal to the long transverse direction (LTD), as shown in Fig. 1, was mechanically polished starting with silicon carbide sandpaper from 320 to 1200 grit before polishing with diamond suspensions of 5, 3, and 1 µm. Final polishing used a 0.05 µm silica colloidal suspension on a vibratory polisher.

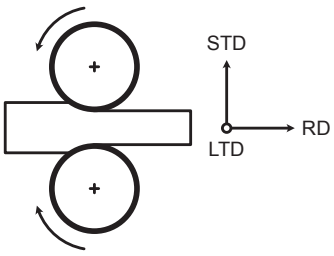

Figure 1: Schematic showing the specimen reference directions after rolling [7].

2.2 SEM image acquisition and processing

EBSD images were acquired at a tilt angle of 70°, using an accelerating voltage of 20 kV at a working distance of 15 mm. Typical fields of view were 585 µm × 520 µm with a step size of 0.5 µm. The EBSD data sets were analyzed using the TSL OIM Analysis software.

BSE images were acquired at three different tilt angles of $-1°$, $0°$, and $+1°$ for each field of interest using an accelerating voltage of 20 kV, probe current of 10 nA, and working distance of 7 mm. All three images were spatially aligned and processed to stretch the contrast in each image using histogram normalization, as described by Bennett and Taleff[6]. All BSE images underwent total variation denoising to reduce the detrimental influence of image noise on the determination of Shannon entropy.

2.3 Calculation of Shannon entropy maps from BSE images

The Shannon[9] entropy H of a population X having s unique values x_i is calculated as

$$H(X) = -\sum_{i=1}^{s} p(x_i) \log p(x_i), \tag{1}$$

where $p(x_i)$ denotes the probability of finding the value x_i in the population, *i.e.*, its number fraction. For example, a population of [a, a, b, c, c, d, e] has $s = 5$ and carries an entropy of 2.24 bits (using base-two logarithm). In the context of a two-dimensional gray-scale (single channel) image, one can define the entropy of each pixel based on the population of intensity values enclosed in a chosen neighborhood around that pixel. In the present study, a square neighborhood of edge length $2N + 1$ is employed that is centered on the pixel.[1] Equation (1) has been implemented as a Python program to calculate the Shannon entropy (in bits) of a given CBSE image by converting it to single-channel gray-scale. Runtimes are proportional to the size of the CBSE image and neighborhood and are typically on the order of minutes.

3 Results

3.1 Parameters for Entropy Calculation

One of the important aspects of this entropy calculation is the window size that is used for the actual calculation. When determining the entropy, we want to make sure that we have an accurate value that accounts for a large enough window without oversupplying data and causing the program to have an excessive runtime. Running the program with window sizes of $N = 2$, 5, 10, and 20 (Fig. 2a–d respectively) we find that at small window sizes ($N = 2$) the grain boundaries are thinner, which is good for segmentation, but overall the data is not accurate enough for any quantitative evaluation due to its high variability. For larger window size ($N > 10$), the data is more continuous and smoother and can be used for analysis. However, the entropy map begins to become blurry due to over-calculation of a pixel and causes future segmentation to be more difficult. Intermediate window sizes such as $N = 5$ provide a good compromise between thin grain boundaries and useful data of the microstructure entropy values.

If we examine the distributions of the entropy values shown in Fig. 3, we can observe a shift in the high-entropy peak to higher values with higher N, which reflects the fact that the theoretical entropy limit is $2 \log (2N + 1)$. Another preliminary parameter was creating bin sizes for the entropy calculation so that gray-scale values that were only differing by a small amount were considered the same in the probability distribution, but it was also found that some data was lost through this process so it was found more efficient to keep the image fidelity at full 8-bit grayscale resolution.

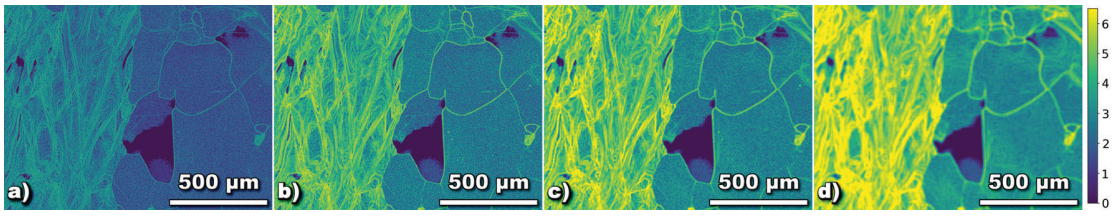

Figure 2: Entropy maps: (a) $N = 2$, (b) $N = 5$, (c) $N = 10$, (d) $N = 20$ from a URX/RX split region from a slice of ATI-40-800 °C.

[1] Window pixels that fall outside of the image are neglected.

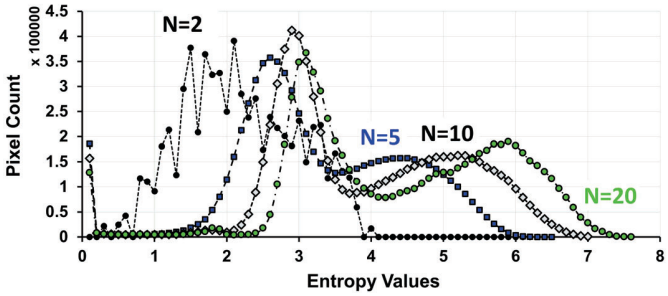

Figure 3: Histogram (pixel count) of entropy values for Fig. 2.

3.2 Entropy distortion caused by noise—importance of sample preparation
Any noise included in the micrographs to be analyzed inflates entropy towards its upper limit since the (local) histogram becomes dominated by the randomness of the noise rather than the structured content. Consequently, entropy no longer measures the structured information of the image but gets skewed to measure the randomness injected by the noise. Ideally, the solution to this is to acquire an image free of noise. However, this can take an excessive amount of time and lead to carbon contamination of the imaged surface. To solve this issue, we first apply Chambolle's algorithm to denoise the image. Even so, when first applying the code to an CBSE image set with recrystallized (RXed) and non-recrystallized (nonRXed) regions (Fig. 4a-c), the BSE image revealed that the surface had not been sufficiently cleaned, with dirt spots throughout the image that locally increased entropy (Fig. 4b). As a result, we did not see the expected bimodal distribution in entropy that we would expect from RXed *vs* nonRXed regions (Fig. 4c). Thus, it is very important to image consistently clean surfaces (Fig. 4d-f).

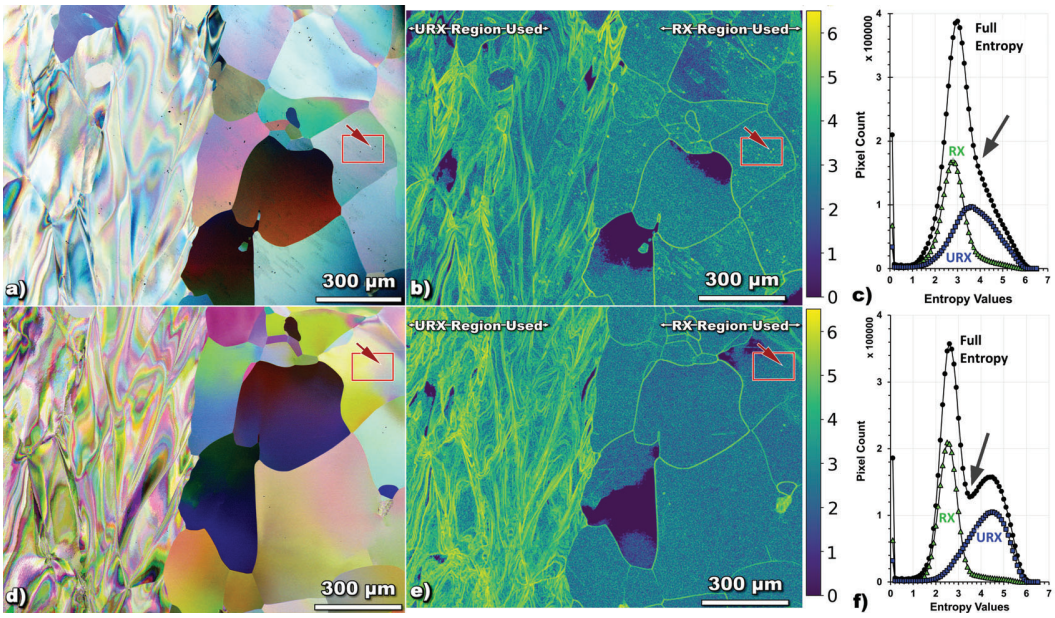

Figure 4: Comparison of insufficient (a–c) and proper (d–f) surface cleaning. CBSE images (a,d) and corresponding entropy map (b,e) with their statistics (c,f). Red rectangles compare same region with (a,b) and without (d,e) speckles left by inadequate polishing. Entropy values are more clearly separable into two distinct distributions for clean surfaces (f). ATI-40 800 °C used as example. Arrows in c) and f) indicate inflection point and valley respectively.

3.3 Entropy variations between RX and URX regions

For the sample image location in Fig. 4d we have an area separated into well-defined regions of URX (left) and RX (right). We also see this in the corresponding entropy map (Fig. 4e). If we plot the entropy distributions (Fig. 4f), we see a clear bimodal distribution with the low-entropy peak representing the RX region and the high-entropy peak the URX region. If we split the image into left and right thirds, we can separately evaluate the entropy of the URX and RX regions. In Fig. 4f we can now clearly see the two separate peaks. We can confirm that RX grains overall have a lower entropy as well as a lower standard deviation of entropy compared to the URX region. From this information, we can clearly see a difference between RX and URX regions and this can be used to find out more about the microstructure that would normally not be possible with BSE images.

3.4 Entropy changes produced after heat treatments

In order to evaluate the use of this program, we then applied it to BSE images for the same Nb sheet heat-treated at different temperatures. Using the 70 % cold work full sheets, we applied heat treatments of 700 °C to 900 °C for 3 h; Fig. 5 shows the resulting entropy maps with corresponding individual BSE images inset.

After applying the entropy program to each temperature image set, we found that the entropy is shifting to lower values overall as temperature increases, as expected for increased levels of recrystallization. Also at the 700 °C heat treatment we find the same bimodal distribution that was in our initial RX/URX sample region, demonstrating the ability of this technique to make RX levels quantifiable. Using the inflection point that the 700 °C and 900 °C relative frequency graphs (Fig. 6) share, we can use this as a cutoff for recrystallization fraction to find the RX fraction to be 70 % for the 700 °C heat treatment, and 94 % for 900 °C (see also Table 1). As observed in Fig. 6, there are high-entropy peaks in the AR and heat-treated cross-sections. Using this present formulation, we cannot distinguish between cold-worked material in AR and possibly recovered or remnant cold work sections after 700 °C, and 900 °C heat treatments. Any distinctions that involve recovery versus cold work would require careful analysis using high-resolution EBSD, which is beyond the scope of the current paper.

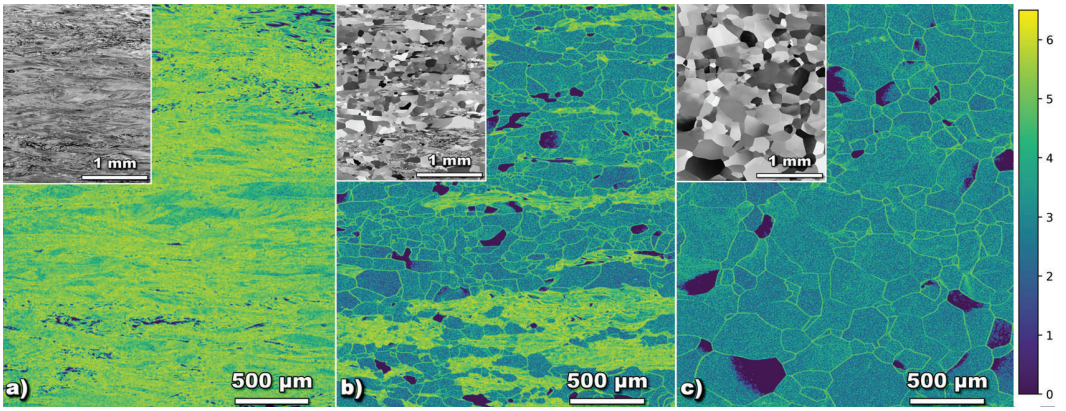

Figure 5: Full-width (vertical) sheet cross-section: ATI-70 % cold work BSE-images as-rolled (a), after 700 °C @ 3 h (b), and after 900 °C @ 3 h (c) with corresponding entropy maps.

Table 1: RX/URX partitioning after different heat treatments (Fig. 5 b,c).

Heat treatment	Fraction	
	RX	URX
700 °C	0.70	0.30
900 °C	0.94	0.06

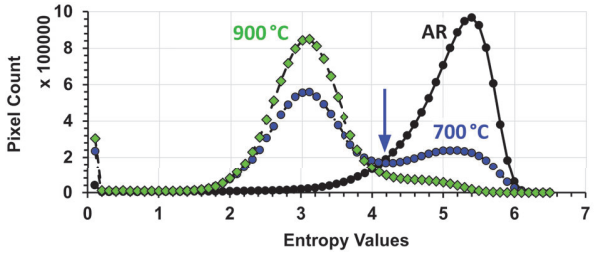

Figure 6: Histogram (pixel count) of entropy values in the maps in Fig. 5. Blue arrow indicates entropy value for count minimum between peaks for 700 °C and inflection point for 900 °C.

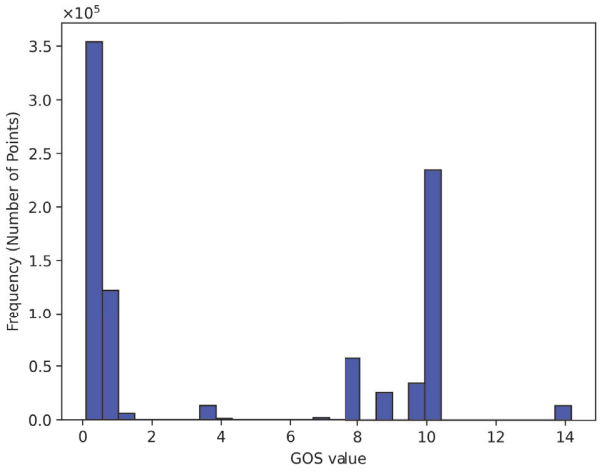

Figure 7: Histogram (data point counts) of GOS values (in degrees) for the region in Fig. 2 with a clear bimodal distribution with a main cutoff at 2°.

3.5 Comparisons of current method with EBSD data

We obtained electron backscatter diffraction (EBSD) data of the region in Fig. 2 and evaluated its grain orientation spread (GOS). The corresponding distribution of GOS values exhibited a clear gap in the vicinity of 2° shown in Fig. 7, which was used to discriminate RX and URX regions of the map by dividing up image pixels with GOS values below and above 2°, respectively. The ensuing partitioning is compared in Table 2 to the outcome resulting from using Shannon entropy as a discriminator. Both evaluations agree closely. The slight difference might be related to the difficulty of discerning the contribution of intermediately high entropy values in the vicinity of grain boundaries that are presently counted towards RX volume and not separated as a third 'species'. In our subsequent investigations we intend to extract the grain boundary information and use this to also determine grain size.

Table 2: Estimation of recrystallized (RX) and unrecrystallized (URX) area fraction in Fig. 2 using either Shannon entropy or grain orientation spread (GOS).

Method	Fraction	
	RX	URX
Shannon entropy	0.61	0.39
EBSD (GOS)	0.56	0.44

4 Conclusions

From our results, we were able to use the Shannon entropy formula to create clear maps that also provides us with values to calculate recrystallization fraction of a region. We also see that EBSD data gives similar data compared to that of entropy data when looking at Grain Orientation Spread data. Completing the entropy calculations takes under 10 minutes, which, combined with the BSE imaging time, is still far under the time it takes to acquire comparable EBSD data. This can provide researchers with a much more cost-effective alternative that can provide basic data about the Niobium surface, which is especially important when evaluating the microstructures from multiple vendors and batches, and from sheets and cavities processed in different ways. Future work will be on optimizing the code to run faster and to also provide grain sizes for the user.

Acknowledgments

This material is based upon work supported by the U.S. Department of Energy Award DE-SC0009960. A portion of this work was performed at the National High Magnetic Field Laboratory, which is supported by National Science Foundation Cooperative Agreement No. NSF-DMR-2128556 and the State of Florida.

References

[1] Posen S, Checchin M, Crawford A, Grassellino A, Martinello M, Melnychuk O, Romanenko A, Ser-gatskov D and Trenikhina Y 2016 *Journal of Applied Physics* **119**(21) 213903. doi:10.1063/1. 4953087

[2] Balachandran S, Polyanskii A, Chetri S, Dhakal P, Su Y F, Sung Z H and Lee P J 2021 *Scientific Reports* **11**(1) 5364. doi:10.1038/s41598-021-84498-x

[3] Khanal B D, Balachandran S, Chetri S, Barron M, Mullinix R, Williams A, Xu P, Ingrole A, Lee P J, Ciovati G and Dhakal P 2024 *Superconductor Science and Technology* **38**(1) 015015. doi: 10.1088/1361-6668/ad9ad7

[4] Raabe D 2014 *Physical metallurgy* pp. 2291–2397. doi:10.1016/B978-0-444-53770-6.00023-X

[5] Humphreys F J and Hatherly M 2004 *Recrystallization and related annealing phenomena* (Oxford: Elsevier) second edition ed. ISBN 978-0-08-044164-1. doi:10.1016 B978-0-08-044164-1.X5000-2

[6] Bennett T J and Taleff E M 2024 *Microscopy and Microanalysis* **30**(5) 913–924. doi:10.1093/ mam/ozae092

[7] Bennett IV T J, Taleff E M, Dhakal P, Balachandran S, Lee P J, Bieler T R and Eisenlohr P 2025 *IEEE Transactions on Applied Superconductivity* **35**(5) 3500805. doi:10.1109/ TASC.2025.3538673

[8] ASTM International: B10 Committee 2018 Standard specification for niobium and niobium alloy strip, sheet, and plate. doi:10.1520/B0393-18

[9] Shannon C E 1948 *Bell System Technical Journal* **27**(3) 379–423. doi:10.1002/ j.1538-7305.1948. tb01338.x